PAPER • OPEN ACCESS

Mode competition in broad-ridge-waveguide lasers

View the article online for updates and enhancements.

Mode competition in broad-ridge-waveguide lasers

J-P Koester[1] , **A Putz**[1] , **H Wenzel**[1] , **H-J Wünsche**[1,2] , **M Radziunas**[2] ,
H Stephan[2] , **M Wilkens** [1] , **A Zeghuzi**[1] **and A Knigge**[1]

[1] Ferdinand-Braun-Institut, Leibniz-Institut für Höchstfrequenztechnik, Gustav-Kirchhoff-Str. 4, 12489
Berlin, Germany
[2] Weierstrass Institute for Applied Analysis and Stochastics, Mohrenstr. 39, 10117 Berlin, Germany

E-mail: Jan-Philipp.Koester@FBH-berlin.de

CrossMark

Abstract

The lateral brightness achievable with high-power GaAs-based laser diodes having long and
broad waveguides is commonly regarded to be limited by the onset of higher-order lateral
modes. For the study of the lateral-mode competition two complementary simulation tools are
applied, representing different classes of approximations. The first tool bases on a completely
incoherent superposition of mode intensities and disregards longitudinal effects like spatial hole
burning, whereas the second tool relies on a simplified carrier transport and current flow. Both
tools yield agreeing power-current characteristics that fit the data measured for 5–23 μm wide
ridges. Also, a similarly good qualitative conformance of the near and far fields is found.
However, the threshold of individual modes, the partition of power between them at a given
current, and details of the near and far fields show differences. These differences are the
consequence of a high sensitivity of the mode competition to details of the models and of the
device structure. Nevertheless, it can be concluded concordantly that the brightness rises with
increasing ridge width irrespective of the onset of more and more lateral modes. The lateral
brightness 2 W mm^{-1}mrad^{-1} at 10 MW cm^{-2} power density on the front facet of the
investigated laser with widest ridge (23 μm) is comparable with best values known from much
wider broad-area lasers. In addition, we show that one of the simulation tools is able to predict
beam steering and coherent beam coupling without introducing any phenomenological coupling
coefficient or asymmetries.

Keywords: high-brightness laser diodes, ridge-waveguide lasers, device simulation,
traveling-wave model, modal analysis, beam steering, coherent mode coupling

(Some figures may appear in colour only in the online journal)

1. Introduction

High power laser diodes based on GaAs and emitting in the
9xx nm range combining a high continuous-wave output
power with a good beam quality are of interest for several
applications, namely, pumping of solid-state and fibre lasers
[1, 2] as well as direct material processing [3].

To enhance the brightness of single emitter laser sources
their output power has to increase at a higher rate than
their beam quality decreases. The achievable output power of
broad-area (BA) lasers has been steadily increased over the
last decades. Their lateral beam quality, however, is dominated
by the appearance of higher-order modes leading to a low
beam quality which limits the achievable brightness [4, 5]. In
contrast, ridge-waveguide (RW) lasers can provide a nearly
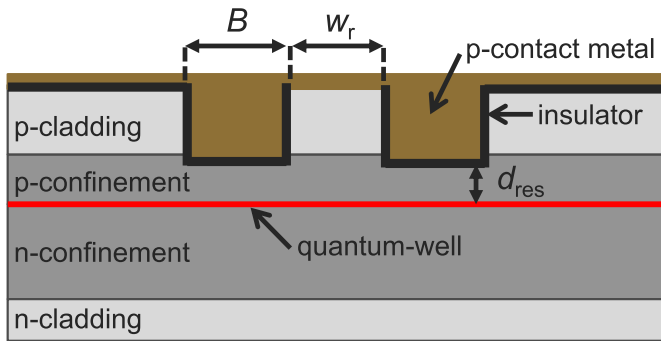diffraction limited beam in combination with output powers

Figure 1. Transverse cross section of a RW laser indicating the n- and p-doped cladding and confinement layers, the insulator as well as the contact metal. In addition the design parameter residual layer thickness d_{res}, the ridge width w_r and trench width B are shown.

in the watt range [6]. Here, the emitted power is limited by the high optical-power density at the front facet as well as thermally-induced power saturation. For a given emitted optical output power those effects can be reduced by enlarging the ridge width. A wider waveguide, however, also increases the chance of exciting higher-order modes. This is especially true far above threshold where spatial hole burning as well as thermal lensing effects become relevant [7, 8].

In this work we study RW lasers as sketched in figure 1 having a weak lateral index guiding combined with the optimized vertical structure of reference [6, 9]. The considered ridge widths of 5, 15 and 23 μm enable us to investigate the transition from single lateral mode operation to the case where several modes contribute to the emitted light. We denote devices in this transition region as broad-ridge-waveguide (BRW) lasers. A better understanding of the partition of power between lateral modes and its impact on the near- and far-field profiles is essential to design laser diodes which combine a large output power with a good beam quality. Simulations based on comprehensive models can provide insights of laser-internal effects not easily accessible by experiments. For this purpose, we compare two different modelling approaches and compare their results to measurements.

One approach is based on an incoherent superposition of the amplitudes of the forward- and backward-propagating waves in the cavity in terms of instantaneous guided modes of the optical waveguide neglecting longitudinal effects as used by several simulation packages [10–12]. We use the tool WIAS-TeSCA representing this modelling approach [13]. In addition, TeSCA is capable to calculate the full (drift-diffusion based) charge carrier transport in the transverse semiconductor cross-section and an arbitrary number of transverse modes in consistence with thermal waveguiding and transverse hole burning.

An alternative way to represent the optical field is to use a time-dependent longitudinal-lateral traveling-wave equation based on the effective-index method as applied by several authors [14–16] without introducing modes *a priori*. This second modelling approach is represented by WIAS-BALaser [17]. Its optical model is coupled to a simplified description of the carrier flow and heat transport adapted to study

BA lasers [4, 5, 18]. Here, it will be evaluated for RW lasers with a much narrower active region.

The fact that TeSCA superposes modes incoherently, i.e. the total optical intensity is the sum of modal intensities, disregards interferences between modes, which are included in BALaser. Comparing simulations with both models will therefore shed light on how important these interferences are. The aim of this paper is to contribute to a better understanding of mode competition by comparing two different models with each other and with measurements.

The remaining paper is organized as follows: First in section 2, we introduce the reader to the laser structure and the underlying design idea. Subsequently, in section 3, we describe the mathematical models behind the simulation tools and discuss their differences. Here we focus on the optical models, which are essential in the context of mode partition. In section 4 we present simulation results of both models and compare with measurements whenever possible. Finally, we summarize and conclude this work in section 5.

2. Design concept and technology

The $Al_xGa_{1-x}As$-based vertical layer structure grown on GaAs comprises a $d_{QW} = 7$ nm thick InGaAs/GaAsP single quantum-well as active region (AR) placed within an extreme double asymmetric (EDAS) large optical cavity (LOC) [19].

The term EDAS refers to a highly asymmetric waveguide design. Here, the compositionally graded index n- and p-confinement layers have a thickness of 3.4 and 0.2 μm, respectively. In addition, the aluminum content is $x = 85\%$ within the p- and $x = 30\%$ within the n-cladding layers. The main advantages of this design are a low electrical series resistance, low carrier leakage and free-carrier absorption lowering electrical and optical losses leading to high conversion efficiencies above 60% [6, 9]. LOC, on the other hand, refers to the high total vertical waveguide thickness of 3.3 μm leading to a decreased optical intensity within the waveguide, which results in an increased catastrophic optical damage threshold. Another advantage is a small vertical far-field divergence. Under pulsed operation the full-width half-maximum of the used vertical design was measured to be 19°. EDAS LOC structures are commonly used in the context of high power laser diodes. By using this vertical structure for BRW lasers a high conversion efficiency can be combined with a good beam quality [6]. However, the exponential decay of the mode field within the thin p-confinement leads to a strong dependence of the strength of the lateral index guiding on the residual layer thickness d_{res}.

The lateral structure was produced by dry-etching pairs of trenches of width B into the p-side of the processed wafer forming the ridge waveguide. Next, silicon nitride was used as insulator covering the areas next to the ridge. Afterwards, a thick Ti–Pt–Au layer was deposited to form the contact and, finally, a gold layer was electroplated on top. A schematic representation of the resulting RW cross section is shown in figure 1. Applying the effective-index method the number of guided lateral modes is mainly governed by the ridge width

w_r and the effective-index step Δn_{eff} which in turn is a function of the residual layer thickness d_{res}. The effective-index step of the investigated devices has been determined to be $\Delta n_{\text{eff}} = 4 \cdot 10^{-3}$.

The lasers were formed by cleaving the processed wafer into 0.4 mm wide and 6 mm long dies forming a Fabry-Pérot resonator between the two ends of the waveguide. The laser facets were passivated and coated with dielectric layers resulting in a front and rear power reflectivity of $R_f = 98\%$ and $R_r = 0.1\%$, respectively.

In what follows we compare measured and simulated results of three device parameter sets having different ridge and index-guiding trench widths, summarized in table 1. Additionally, the number of guided 1D lateral modes is added assuming infinitely extended trenches and a cold and unbiased waveguide. In the following text we refer to the different parameter sets by simply calling them designs 1, 2 and 3, respectively.

3. Electro-optical-thermal simulation models

Here, we introduce the two simulation tools WIAS-TeSCA [13] and WIAS-BALaser [20] as representatives for a number of tools mentioned in the Introduction. In what follows we first sketch the common framework of both tools and emphasize afterward their differences. Thereby we focus on the different concepts of modes being the subject of this paper. As to other components we refer to literature.

3.1. Theoretical framework

In the present case of Fabry–Perot lasers with TE polarization, the main component of the electrical field within the laser resonator is expressed as:

$$\vec{E}(x,y,z,t)$$
$$= \frac{1}{2}\boldsymbol{e}_x \left[E^+(x,y,z,t)e^{-i\beta_0 z} + E^-(x,y,z,t)e^{i\beta_0 z} \right] e^{i\omega_0 t} + \text{c.c.}$$
(1)

Here, x and y are the transverse (lateral and vertical, respectively) coordinates, $\boldsymbol{e}_x$ is a unity vector ($\parallel x$), $E^{\pm}$ are complex-valued amplitudes varying slowly along the cavity axis (longitudinal coordinate z) and with respect to time t, β_0 is a real-valued reference propagation constant, ω_0 is the central angular frequency, and c.c. denotes complex conjugate. The slow amplitudes obey the paraxial equations, formula (27.86) in [21],

$$\left(\frac{-2i\beta_0}{v_g}\frac{\partial}{\partial t} \mp 2i\beta_0\frac{\partial}{\partial z} + \frac{\partial^2}{\partial^2 x} + \frac{\partial^2}{\partial^2 y} + k_0^2\varepsilon - \beta_0^2 \right) E^{\pm}$$
$$= F_{\text{sp}} - \mu_0\omega_0^2 e^{\pm i\beta_0 z}P_{\text{disp}}$$
(2)

with $k_0 = \omega_0/c_0$, where c_0 is the speed of light in vacuum. Reflecting boundary conditions hold at the facets and appropriately mixed boundary conditions at the transverse boundaries. A common group velocity v_g of all components of the internal laser radiation is assumed. Expressions of reference

Table 1. Lateral parameter of the investigated RW laser, namely, ridge width w_r and index trench width B. The last column shows the number m of lateral modes guided by the cold waveguide.

Design	w_r μm^{-1}	B μm^{-1}	m
1	5	8	2
2	15	3	6
3	23	2	8

[21] are used for the stochastic Langevin force F_{sp} of spontaneous emission and the dispersion contribution to the optical polarisation P_{disp}. $\varepsilon(x,y,z,t,\mathcal{P})$ is the dielectric function at central frequency ω_0. It is locally composed of refractive index $\bar{n}$, gain g and absorption coefficient α according to $\varepsilon = (\bar{n} + i\frac{g-\alpha}{2k_0})^2$ ε depends on parameters $\mathcal{P}$ representing the device structure, material parameters, as well as the distributions of electrons, holes and temperature possibly slowly varying with time.

The distribution of charge carriers in the device is commonly obtained from the van Roosbroeck system consisting of drift-diffusion equations for the electron and hole densities $n(x,y,z,t)$ and $p(x,y,z,t)$, respectively, and the Poisson equation of the electrostatic potential φ [22]. The optical field enters via the rate of stimulated recombination $R_{\text{st}} \sim \bar{n}g(|E^+|^2 + |E^-|^2)$, thus neglecting the interference between forward and backward propagating waves. The distributions of gain, refractive index and other parameters depend sensitively on the temperature distribution $T(x,y,z,t)$ within the laser cavity which is determined by the heat-flow equation as extensively described in, e.g. references [13], [21], and [5].

Although already based on several approximations, this high-dimensional non-linear system is still impracticable for realistic device structures composed of a lot of different materials with a complex geometry. Further complimentary approximations of our two models will be described separately in what follows.

3.2. TeSCA

Similarly as in other simulation packages like LASTIP [10], LaserMOD [11], and Harold [12] in TeSCA the amplitudes of the forward and backward propagating fields are expanded in terms of the instantaneous and longitudinal invariant guided modes of the optical waveguide. For present purposes, we have created an extension of TeSCA [13] taking into account an arbitrary number of modes.

The instantaneous modes are solutions of equation (2) with its right hand side set to zero. Assuming longitudinal invariance and constance of the parameters $\mathcal{P}$, in particular neglecting longitudinal spatial hole burning, the modes can be calculated by a separation of variables with the Ansatz

$$E_{k\nu}^{\pm}(x,y,z,t,\mathcal{P}) = A_{k\nu}(t)f_k^{\pm}(z)\Phi_\nu(x,y,\mathcal{P}).$$
(3)

The transverse mode $\Phi_\nu(x, y, \mathcal{P})$ is the normalized solution of the eigenvalue equation

$$\left[\frac{\partial^2}{\partial x^2} + \frac{\partial^2}{\partial y^2} + \frac{\omega_0^2}{c_0^2}\varepsilon(x, y, \mathcal{P})\right]\Phi_\nu(x, y, \mathcal{P}) = \beta_\nu^2(\mathcal{P})\Phi_\nu(x, y, \mathcal{P}).$$
(4)

The longitudinal amplitude distributions are fixed by the reflecting boundary conditions,

$$\begin{pmatrix} f_k^+(z) \\ f_k^-(z) \end{pmatrix} = a \begin{pmatrix} r_r e^{-iq_k z} \\ e^{+iq_k z} \end{pmatrix} \quad \text{with} \quad q_k = k\frac{\pi}{L} - \beta_0 - \frac{i}{2\,L}\ln(r_r r_f).$$
(5)

The integer index k labeling longitudinal modes represents the number of half waves in the resonator. The normalization constant a can be chosen independent of k such that $|A_{k\nu}|^2$ is the mean power of mode $k\nu$ in the resonator. The temporal variation is obtained to follow

$$\frac{dA_{k\nu}}{dt} = i\Omega_{k\nu}(\mathcal{P})A_{k\nu} \quad \text{with}$$

$$\Omega_{k\nu}(\mathcal{P}) = v_g\left(k\frac{\pi}{L} - \beta_\nu(\mathcal{P}) - \frac{i}{2L}\ln(r_r r_f)\right),$$
(6)

where $\frac{\beta_\nu^2 - \beta_0^2}{2\beta_0} \approx \beta_\nu - \beta_0$ has been used exploiting $|\beta_\nu - \beta_0| \ll \beta_0$. The real part of $\Omega_{k\nu}$ is the mode frequency relative to ω_0 and the imaginary part is a decay rate. When expanding the fields $E^\pm$ in equation (3) into a sum of modes, the intensity being quadratic in $E^\pm$ contains nondiagonal interference terms beating with the differences between mode frequencies. TeSCA averages out all beating terms, supposing that the beating periods are much smaller than other opto-electronic and thermal time scales. This condition is fulfilled in sufficiently short lasers with not too weak lateral waveguides. Then, the longitudinally averaged stimulated recombination is governed by the intensity

$$S(x, y, t) = \sum_\nu P_\nu(t)|\Phi_\nu(x, y, \mathcal{P})|^2.$$
(7)

The mean transverse-mode power $P_\nu(t) = \sum_k |A_{k\nu}|^2$ includes the contribution of all longitudinal modes of the given transverse mode ν. Thus, one arrives at one single equation of motion for each transverse mode,

$$\frac{dP_\nu}{dt} = G_\nu P_\nu + \dot{P}_{\text{sp},\nu} \quad \text{with}$$

$$G_\nu = v_g\left(2\text{Im}[\beta_\nu(\mathcal{P})] - \alpha_{\text{out},\nu} - \alpha_{\text{s},\nu}\right).$$
(8)

$\alpha_{\text{out},\nu} = -\ln(|r_r r_f|)/L$ and $\alpha_{\text{s},\nu}$ are the out-coupling (mirror) losses and possible additional scattering losses, respectively. Expressions for the power $\dot{P}_{\text{sp},\nu}$ emitted per unit time due to spontaneous emission into mode ν as well as for other quantities not specified here can be found in reference [13].

Although TeSCA can handle time-dependent problems, we restrict ourselves here to the stationary case appropriate for CW operation. A stationary solution exists even in the multimode case due to neglecting beating terms in the series (7). The complex eigenvalue problem (4) is approximately solved

as follows: The finite element discretization creates a complex matrix, the real part of which is symmetric and positive definite. For this real part, the eigenvalues and eigenfunctions are calculated using Arnold iterations. Both, eigenvalues and eigenfunctions, are real. Then the imaginary parts of the eigenvalues $\text{Im}[\beta_\nu^2]$ are calculated as first-order perturbation. This procedure is carried out iteratively in a self-consistent manner and in parallel with the calculation of the carrier densities and the temperature. Since the spontaneous emission into a single transverse mode $\dot{P}_{\text{sp},\nu}$ is extremely small, a mode ν can reach a noticeable stationary power P_ν only if its net gain G_ν is very close to threshold $G_\nu = 0$.

3.3. BALaser

In BALaser, $\varepsilon(x, y, z, t, \mathcal{P})$ is allowed to vary also in longitudinal direction z. Similarly as applied by other authors [14–16], the following Ansatz is employed for the forward and backward propagating field amplitudes:

$$E^\pm(x, y, z, t) = a'\phi(y)u^\pm(x, z, t).$$
(9)

$\phi(y)$ represents the normalized fundamental vertical mode profile and the constant a' is chosen such that $|u^+|^2 + |u^-|^2$ is a photon density. Using this ansatz equation (4) is solved by dropping the lateral derivative,

$$\left[\frac{\partial^2}{\partial y^2} + k_0^2\varepsilon(x, y, z, \mathcal{P})\right]\phi(y) = k_0^2\bar{n}_{\text{eff}}^2(x, z)\phi(y).$$
(10)

The parametric dependence of $\phi(y)$ and of the effective index $\bar{n}_{\text{eff}}$ is not indicated here for brevity. Inserting (9) into (2), multiplying with $\phi(y)$ and integrating over y, we obtain the travelling-wave equations (TWE)

$$\left[\frac{n_g}{c}\frac{\partial}{\partial t} \pm \frac{\partial}{\partial z} + \frac{i}{2\beta_0}\frac{\partial^2}{\partial x^2}\right]u^\pm = -i(k_0\Delta\bar{n}_{\text{eff}} + \mathcal{D})u^\pm + f_{\text{sp}}^\pm$$
(11)

subject to reflective boundary conditions. $\Delta\bar{n}_{\text{eff}} = \frac{k_0^2\bar{n}_{\text{eff}}^2 - \beta_0^2}{2\beta_0 k_0} \approx \bar{n}_{\text{eff}} - \beta_0/k_0$ is the relative effective index, $\mathcal{D}$ is an operator accounting for the dispersion contribution to the polarization, and $f_{\text{sp}}^\pm$ are Langevin forces derived from F_{sp}. The transport and heat equations are treated as described in reference [5].

In contrast to the transverse modes in TeSCA, WIAS-BALaser presets only the vertical variation of the optical field by the fundamental mode $\phi(y)$ of the strong vertical waveguide. Laterally, modes are formed here only implicitly by the interplay between the lateral diffraction and the weak waveguide established by $\Delta\bar{n}_{\text{eff}}$ in (11). To study mode competition and to get results comparable with TeSCA, we apply a post-processing mode analysis similar to the one described in reference [4].

3.4. Model comparison and parameter adaption

This paper aims at a better understanding of mode competition by comparing two sophisticated models with each other
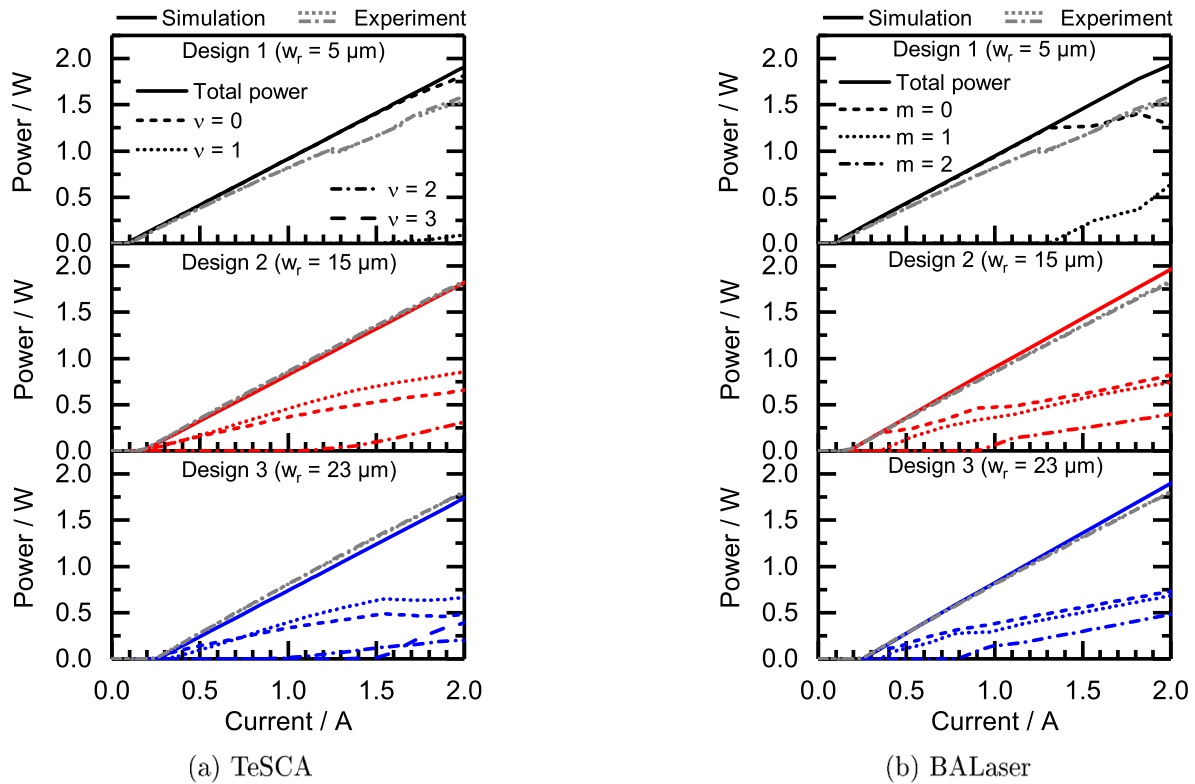
Figure 2. Power-current-characteristics obtained by (a) TeSCA and (b) BALaser. The top, middle and bottom part of each plot shows the corresponding results of design 1, 2 and 3, respectively. The total emitted power is represented by solid lines for the calculated and gray dotted/dash-dotted lines for the two measured lasers of each design. Other line styles represent the modal powers according to the legend.

and with measurements. Whenever possible, identical simulation parameters are selected, taking into account the differences between the two models presented. A summary of the model characteristics is shown in table 2. Most of the parameters entering the simulation models were taken from literature [23], [24]. The effective densities of states of the quantum well as well as the dependence of the refractive index on the carrier density were fitted to the results of a microscopic calculation [25]. The dependence of the parameters on the internal temperature (higher than the heat sink temperature due to the self-heating) is given in [26]. The optical losses due to free-carrier absorption were calculated using the cross-sections $4 \cdot 10^{-18}$ cm^2 and $12 \cdot 10^{-18}$ cm^2 for electrons and holes, respectively, in both of the bulk layers and in the quantum well. In order to be close to the experimental structures, the lifetimes due to Shockley-Read-Hall recombination and the pre-factor of the local gain function were used as parameters to fit the results of the length dependent measurements of threshold current and slope efficiency of BA lasers operated under pulsed operation using a one-dimensional simulation as described in [9]. Subsequently, the scattering loss parameter α_s used in TeSCA was adjusted to reach a good agreement of the slope slightly above threshold with the measured power-current characteristics of design 1 with $w_r = 5$ μm (see figure 2(a)). A similar adaptation was not needed in the case of BAlaser (see figure 2(b)).

To achieve a good agreement of the thermal profiles obtained by both simulation tools an additional adaption was required. The reasons are differences in their thermal models as well as the size of the considered computational domain. BALaser incorporates not only all semiconductor parts of the device but also all other materials between semiconductor and heat sink. Additionally, the full 400 μm width of the laser chip is taken into account. TeSCA, however, resolves only a restricted part of the vertical semiconductor layer structure. The same applies for the lateral domain which is limited to about 45 μm due to convergence problems. The heat-flow at the resulting boundaries is defined via heat transfer coefficients.

The amount of self-heating was adjusted to result in an approximately 5 K rise of temperature per 1 W emitted output power in the waveguide center ($x = 0$) at the front facet (c.f. figures 3 (e) and (f)). In both tools, this was achieved by properly choosing the vertical heat transfer coefficient to the heat sink entering a mixed boundary condition at the top (p-down mounting) and homogeneous Neumann conditions at the bottom. Next, the lateral heat transfer coefficients in TeSCA were chosen such that the obtained lateral thermal profile approached that of BALaser using a 400 μm wide lateral domain with homogeneous Neumann conditions for a fixed ridge width and optical power. Here, special care was taken to achieve the same lateral temperature gradient around the ridge edges.

Table 2. Model comparison.

Model	TeSCA	BALaser
Optical field	Incoherent superposition of transverse modes, full cross-section	Inplane travelling waves, Effective-index method
Drift-diffusion of carriers	Exact equations, full cross-section	Diffusion and Laplace equations, active and p-doped regions
Temperature flow	Same domain and mesh as for carriers	Larger domain as for carriers and different mesh
Longitudinal averaging	Yes	No

4. Time-averaged characteristics of few-lateral mode CW operation

Under continuous-wave (CW) operation a laser is driven under constant conditions leading to an output which is constant in time. However, a light wave is always emitted, which is a spatio-temporal dynamical phenomenon. Furthermore, the omnipresent noise causes temporal fluctuations. In case of multiple modes in the spectrum, their beating creates additional temporal variations of the intensity. Nevertheless, all these dynamics usually occur on extremely short sub-ns time scales whereas intensities are averaged over much longer but still short mesoscopic times and can thus be regarded as time-constant under CW operation. This averaging is done differently in the two simulation tools. TeSCA bases on equations directly for averaged quantities and reaches a true constance under constant conditions. BALaser on the other hand exploits equations that involve short-time dynamics. Here, the averaging has to be done in a post-processing step. It is one goal of this section to compare the results of the two averaging procedures. We present simulation results for all three ridge widths $w_r = 5, 15$, and $23\,\mu$m obtained at a constant heat-sink temperature of 25 °C. Thereby, we focus on different aspects of few-mode operation. Whenever possible we compare the simulations with measurements.

4.1. Power-current characteristics

Plotting the emitted mean power *P* versus the mean pump current *I* in CW operation is one of the most basic and often measured laser characteristic. In figure 2, calculated and measured PI curves are opposed to each other for all investigated designs (see table 1). The total powers obtained by both simulation tools show a satisfactory agreement with each other and with the two nominal identical lasers measured for all three designs. Only the bending of the measured curve for design 1 is not completely reproduced by the simulations, which have neglected scattering losses at the side walls of the ridge. This small discrepancy is not important for the purpose of the present paper.

The mode competition within the laser is represented by the modal resolved powers plotted as dashed and dotted lines. Both models agree qualitatively also in this respect. Design 1 is dominantly single mode in the investigated range of currents. The other designs, having wider ridges, are dominantly

multimode, whereby the number of lasing modes tends to increase with ridge width. All transverse TE$_{\nu 0}$ modes $\Phi_\nu(x,y)$ lasing in TeSCA have ν vertical null lines (not shown). Their spatial structure within the AR is thus the same than the lateral modes of BALaser with corresponding *m*. It is noteworthy that for all designs the number of lasing lateral modes is equal or less than supported by the corresponding cold and unbiased waveguide (c.f. right most column of table 1). Each mode has its individual threshold current and its power contribution grows smoothly above it.

There are also differences between the models. Higher modes appear at slightly different currents. The powers of the first two modes are reversed in the two designs with wider ridges. In the case of TeSCA and design 3, an additional (third higher-order) mode exceeds threshold but not in the BALaser simulations. Unfortunately, we have no experimental data on individual modal powers to compare with. Thus, we cannot decide which model is better in this respect. Nevertheless, the differences between the two models are small and we believe that both simulations provide a deep and reliable insight into the mode competition, which is not simply obtainable from measurements.

It is interesting to note that these differences occur even in cases where the total powers agree with each other. The partition of the total power over co-lasing modes is clearly much more sensitive to details of the models than the total power itself. This phenomenon is known since the early days of semiconductor lasers in the context of mode partition noise [27–30]. It is an intrinsic property of laser physics and cannot be circumvented. Co-lasing of different modes requires that the round-trip gain of each mode equals its round-trip losses. It is this subtle balance that depends very sensitively on the carrier and temperature distributions.

4.2. Spatial distributions in the single-mode regime

The onset of higher-mode lasing is closely related to spatial hole burning. The different representations of this effect by the two models are compared in figure 3 for laser design 1 at 1 W output power, before the first higher-order-lateral mode starts lasing.

Left panels show the distributions of intensity, excess carrier density, and temperature in the transverse cross section as calculated by TeSCA. The lateral-longitudinal distributions of the same quantities vertically averaged over the AR,
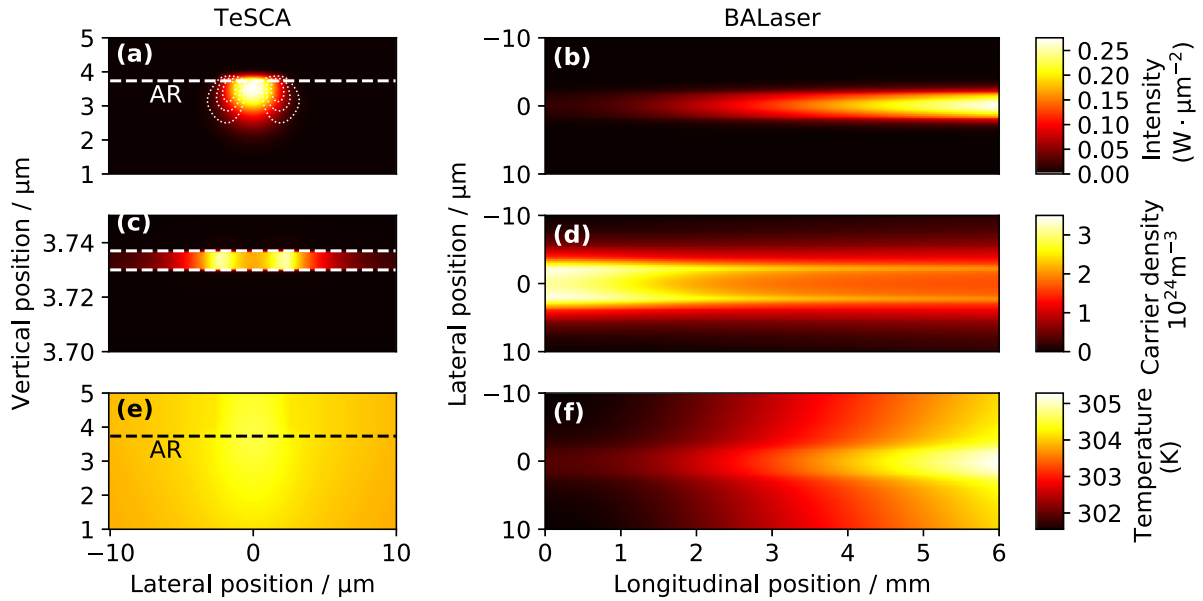
Figure 3. Calculated spatial distributions of the laser with 5 μm ridge width at 1 W optical output power. AR indicates the active region. The left panels (a), (c), (e) are the intensity, the excess carrier density in the AR, and the temperature, respectively, calculated with TeSCA. The thin white dotted lines in panel (a) are contour lines of the second transverse mode, which is still below threshold here. The vertical scale in panel (c) is zoomed to resolve the thin AR. Right panels (b), (d), (f) are the mean intensity, excess carrier density, and the temperature within the AR, respectively, calculated with BALaser. The color bars belong to both models.

as calculated with BALaser are shown in the right panels. The intensity distribution of panel (a) is laterally confined by etched ridges (see figure 1). In addition, it reflects clearly the extremely asymmetric vertical EDAS structure. Most of the power is guided below the AR and only $\Gamma_y = \int_{-d_{QW}/2}^{d_{QW}/2} |\phi(y)|^2 dy / \int |\phi(y)|^2 dy = 0.62\%$ is confined within the AR. Nevertheless, the intensity in the AR is still high and its stimulated recombination burns a deep lateral hole in the excess carrier distribution (panel (c)). The fundamental mode overlaps most with the center of the carrier distribution. It is kept lasing by the gain provided by the carrier density of slightly above 2×10^{24} m^{-3}. The much higher densities near the borders of the ridge overlap much better with the first higher-order mode illustrated by the thin dashed lines in panel (a). This fact reduces the difference in gain of the latter mode relative to the fundamental one, bringing it also close to threshold. With increasing current, the gain difference will further decrease until this mode lases, too. Its additional stimulated recombination will keep its gain at threshold when further raising the current. During this process, the distributions of excess carriers as well as temperature (panel (e)) change in a subtle way such that the gains of both active modes are kept at threshold.

Turning to the right panels, we see a comparable lateral hole burning in the results of BALaser. However, in addition to the TeSCA case, the intensity varies strongly in the longitudinal direction and, as a consequence, also the depth and shape of the lateral carrier density hole as well as the distribution of temperature. Obviously, this strong longitudinal hole burning affects the mode competition. In particular, the fundamental mode experiences large gain only within few millimeters from the left facet. In contrast, the high inversion at the ridge borders is

extended over the full length of the laser. This feature overlaps best with the first higher-order mode and can explain why it is lasing earlier in BALaser than in TeSCA where longitudinal hole burning is neglected. The use of a laterally constant confinement factor in the framework of BALaser further enlarges this effect. The lower refractive index of top layers outside the ridge makes the vertical confinement Γ_y smaller. Thus, the overlap with the excess gain at and beyond the ridge boundary is overestimated by BALaser further favoring the first higher-order mode. This effect is only marginal in BA lasers for which the tool BALaser has been developed. Future applications of BALaser to small contact widths should however use an appropriate $\Gamma_y(x)$.

4.3. Near fields

The measurement of the so called near field, i.e. the spatial distribution of the time-averaged optical intensity on the front facet, is one of the standard methods to characterize the emission quality of semiconductor lasers. The lateral near-field distributions $|E_{NF}(x)|^2$ of two devices of each design have been measured and plotted in figure 4(c). Although the device pairs are nominally identical, they exhibit quite different near fields, in particular in the regime of multimode operation. This fact again underscores the high sensitivity of the mode competition, here, caused by the always present small differences between any two real devices. In particular, small lateral asymmetries not present in the models transform into noticeable asymmetries of the measured near fields, whereas all calculated near fields stay symmetric, figures 4(a) and (b). An evaluation of the theoretical near fields by comparing with experimental ones is difficult under these
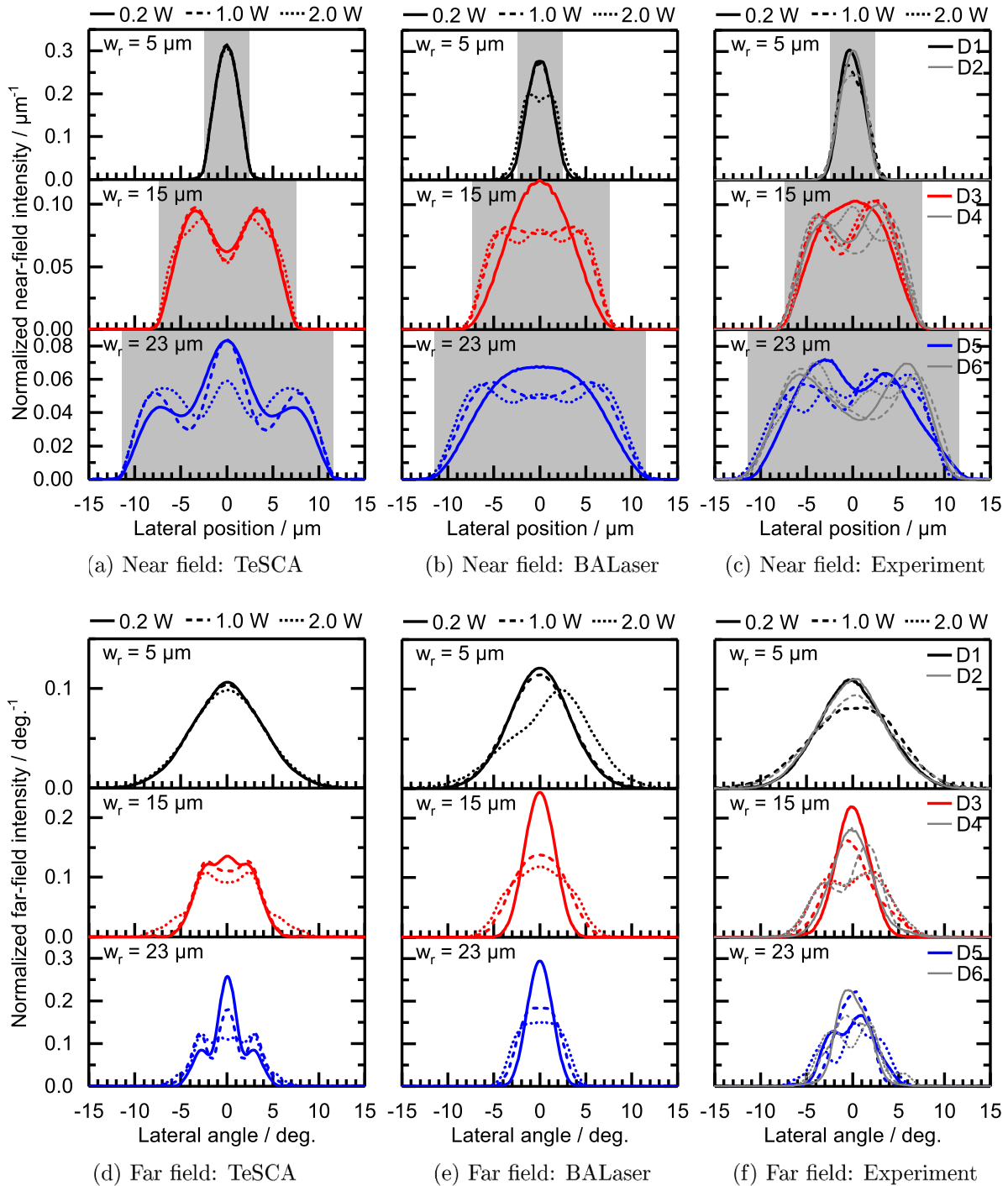
Figure 4. Normalized lateral intensity profiles of the near field (a), (b), (c) and far field (d), (e), (f) of lasers emitting 0.2 W (solid lines), 1.0 W (dashed lines) and 2.0 W (dotted lines) obtained by (a), (d) TeSCA, (b), (e) BALaser and (c), (f) experiment. The top, middle and bottom part of each plot shows the results of designs 1, 2 and 3, respectively. The gray box in the near-field plots represents the design ridge width.

circumstances. Nevertheless, despite all necessary caution, we can observe the following tendencies. The number of maxima is identical in all cases. This means the number of co-lasing modes agrees between both models and experiment. With respect to their shape, the near fields of BALaser are more

similar to the measured ones. They have a similar modulation depth whereas the TeSCA fields are distinctly deeper modulated. We conclude that BALaser tends to describe the near field better than TeSCA, perhaps due to the incorporation of the longitudinal hole burning.
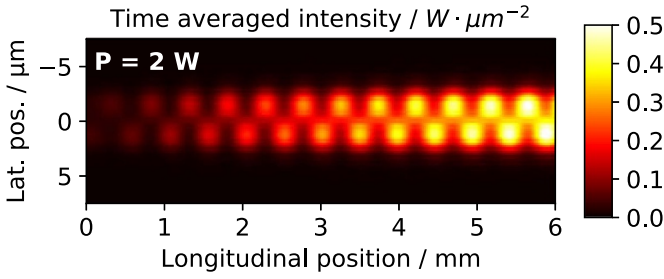
Figure 5. Time averaged longitudinal-lateral mean intensity distribution within the active region calculated with BALaser for design 1 at $P = 2$ W.

4.4. Far fields

The angular distribution of the far-field intensity emitted by the laser is a further important characteristic. It is calculated from the complex near-field amplitudes via Fourier transformation and has been directly measured for all samples. The corresponding time-averaged lateral far-field distributions are shown in figures 4(d)–(f). Simulations and experiment agree in following respects. All far fields for the most narrow ridge are single lobed. They get more structured and become narrower with increasing ridge width. The beam divergence increases with increasing power in all cases. However, also differences are seen.

First of all, the far fields of the nominally identical experimental sample pairs differ from each other as did their near fields in figure 4(c). Again, this reflects the high sensitivity of the balance between multiple lasing modes.

Second, the smoothness of the BALaser curves for wide ridges is in striking contrast to TeSCA and experiment. It is due to the applied kind of temporal averaging. The far-field amplitude is calculated in each time instant from the actual near-field amplitude and the intensities are averaged thereafter over time. The instantaneous intensities (not shown in our figures) exhibit structures reflecting their modal content. However, these structures undergo mode beating variations, which are smoothed out by the temporal average. TeSCA in contrast calculates the far-field intensities of the individual modes and superimposes them incoherently. This yields fully structured far-field curves. The experimental averaging is similar to BALaser but structures imposed by imperfections can survive the averaging.

Third striking peculiarity is that BALaser predicts a steered far field with a maximum at $\theta \approx 2.2°$ for design 1 at 2.0 W, although the laser structure is fully symmetric. The internal time-averaged intensity distribution within the resonator is shown in figure 5. It exhibits a distinct spatial modulation. Such stationary meanders have been discussed already in the contexts of kinking and beam steering [31–33]. They are the coherent superposition of lateral mode pairs with different longitudinal mode indexes k_1 and k_2 but identical frequencies $\Omega_{k_1,1} = \Omega_{k_2,2}$. According to equation (5), the intensity of this coherent superposition contains a mixed term that oscillates along z with the spatial frequency $(k_1 - k_2)\pi/L$, corresponding to $(k_1 - k_2)/2$ periods along the cavity. The mixed term

is also proportional to the antisymmetric factor $\psi_1(x)\psi_2^*(x)$ and, thus, its maxima occur alternately on the left and right sides of the ridge. As the asymmetric field amplitude of the meander on the front facet is stationary, the far field gets asymmetric as seen in the upper panel of figure 4(e). Quantitatively, we find $k_1 - k_2 \approx 25$ from figure 5. According to equation (6), the frequencies of the two lateral modes thus agree if $\beta_1 - \beta_2 = (k_1 - k_2)\pi/L \approx 1.31 \cdot 10^4$ m^{-1}. This coincides well with $\beta_1 - \beta_2 = 1.2955 \cdot 10^4$ m^{-1} obtained by our mode calculation. This type of beam steering often occurs together with a kink in the power-current-characteristics. In practice, this is caused by a reduced laser-detector or laser-fiber coupling. However, our simulations did not consider a finite detector aperture and no kink is seen in figure 2(b). Finally we note that the time dependent intensity within the resonator is not spatially constant but varies in time. The stationary meander-like intensity distribution gets revealed by an averaging over time. However, a deeper analysis of this behaviour as well as of other dynamical effects is beyond the scope of present paper and is intended to be reported elsewhere.

The fact that even measured near- and far-field profiles obtained for two lasers of the same design in most cases did not agree, indicates that already small perturbations within those devices are enough to obtain distinctly different results. The same argument also holds for the differences between both simulation tools.

4.5. Beam parameter product and brightness

The lateral beam parameter product BPP$_{lat}$ is a commonly used measure of the beam quality of laser diodes and of major importance for many applications. It is defined as the product of the lateral beam radius and the beam divergence:

$$\text{BPP}_{lat} = \frac{w_{95\%}}{2}\frac{\theta_{95\%}}{2}, \tag{12}$$

where $w_{95\%}$ is the full lateral near-field width (carrying 95% of the power) and $\theta_{95\%}$ the corresponding full lateral far-field angle. In figure 6 the BPP$_{lat}$ is shown as function of the emitted optical output power up to 3 W. Here, the simulations show a reasonable agreement with the experiment for designs 1 and 2. The laser with the smallest ridge width resulted for all powers in a BPP$_{lat}$ close to the theoretical minima of $\lambda_0/\pi \approx 0.3$ mm. Design 2 shows a declining beam quality up to 1 W output power but a nearly constant BPP$_{lat} \approx 0.6$ thereafter. However, laser design 3 with $w_r = 23$ μm shows an increasing BPP$_{lat}$ over the full power range indicating a rising number of power contributing higher order lateral modes.

The lateral brightness B_{lat} defined as the ratio of the emitted optical output power P and the lateral beam parameter product BPP$_{lat}$ is an ideal figure of merit to compare the performance of lasers with different ridge widths. To increase B_{lat} the power has to rise at a higher rate than the beam quality declines. However, the output power of a given laser can not be increased endlessly. This has two main reasons. First, self heating lowers the conversion efficiency which further increases the power dissipation leading to even higher
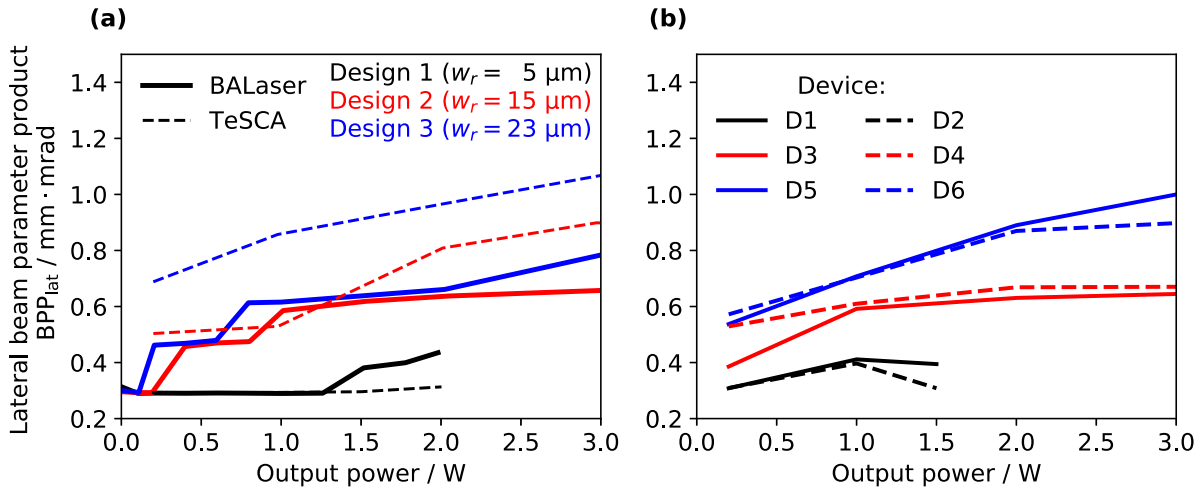
Figure 6. Lateral beam parameter product BPP$_{lat}$ as function of the emitted optical power *P* obtained by simulations (a) and experiments (b) for designs 1, 2 and 3.
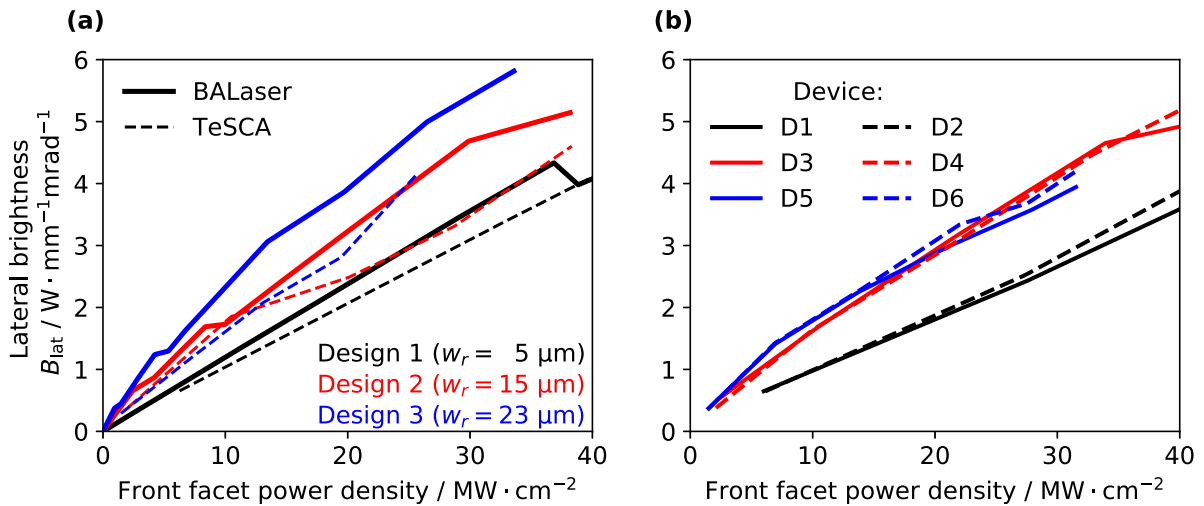

Figure 7. Lateral brightness of the emitted beam as function of the power density *S* at the front facet obtained by simulations (a) and experiments (b) for designs 1, 2 and 3.

device temperatures. Second, the power density at the facets increases. Both effects play a major role in the context of catastrophically optical mirror damage (COMD). However, COMD is a very complex process being still under research [34–37].

We assume that a COMD event is proportional to the power density S_f at the front facet, which we estimate according to

$$S_f = \frac{P}{w_y w_x} = P \left[\frac{(\int |\phi(y)|^2 dy)^2}{\int |\phi(y)|^4 dy} \frac{(\int |E_{NF}(x)|^2 dx)^2}{\int |E_{NF}(x)|^4 dx} \right]^{-1} . \quad (13)$$

w_x and w_y are effective lateral and vertical beam widths, respectively. The latter is calculated based on the fundamental vertical mode $\phi(y)$ obtained by equation (4). The lateral effective beam widths are calculated considering lateral near-field profiles $|E_{NF}(x)|^2$ as shown in figures 4(a)–(c).

A COMD may happen if *S* exceeds a certain threshold. This threshold is not precisely known but it can be expected to be in the order of 10–100 MW cm^{-2}. In this context, it makes

sense to plot B_{lat} versus S_f which is growing with an increasing pump current. These curves calculated and measured for the investigated devices are collected in figure 7. The curves for $w_r = 5\,\mu$m (black) are straight lines because the near field is single mode and does not change much with increasing power. Both measurements and calculations agree reasonably with each other. The next larger ridge width enhances the brightness curve distinctly and visibly, again with reasonable agreement between experiment and simulation with BALaser. TeSCA fails here to predict the experimental results. The curves for $w_r = 23\,\mu$m, however, disagree between both simulation tools and measured values. Here, in particular BALaser predicts a larger brightness than measured, caused by a smaller far-field divergence (c.f. figure 4(e) This is in agreement with previous results obtained for multi-mode BA laser [18].

It is interesting to compare between BRW lasers and BA lasers with respect to their brightness at a given front power density. Measured data of BA lasers with a comparable vertical structure are available for $S \approx 10$ MW cm^{-2}

in reference [38] ('reference' in table 1 therein). They are $B_{\text{lat}} = 2.62, 2.45,$ and 2.20 W mm^{-1}mrad^{-1} for stripe widths of $50, 90,$ and $186\ \mu$m, respectively. These values only marginally exceed those of our values measured for ridge widths 15 and 23 μm and they seem to decrease slightly with stripe width. From this fact we can draw two conclusions. First, the transition from narrow single-mode RW lasers via multimode BRW lasers towards BA lasers is accompanied by a noticable rise of the brightness at a given front facet power density. This rise already begins to saturate in the domain of BRW laser due to the appearance of more and more lateral modes. The second conclusion is: BRW lasers can reach brightness values comparable to those of BA lasers.

5. Summary and conclusion

In this paper we studied the transition from single- to multi-mode emission in CW driven RW lasers at different power levels and increasing ridge width. This was done by comparing simulation results of WIAS-TeSCA and WIAS-BALaser, which rely on different mathematical modelling approaches, with those of selected experiments.

Both simulation tools showed good agreement with the experimental power-current characteristics. Furthermore, a good qualitative conformance of the near and far field with the experiment was found. The specific profiles for each ridge width and power level, however, showed variations between each simulation tool, caused by only slight deviations of the predicted modal power fractions and lasing thresholds. The fact that even measured near- and far-field profiles obtained for two lasers of the same design did not agree indicates that already small perturbations or differences within those devices or of the simulation tools are enough to obtain distinctly different results. Additionally, we could show that BALaser is able to predict beam steering and coherent beam coupling without introducing any phenomenological coupling coefficient or asymmetries.

In addition, it could be shown that the brightness for a given front facet power density can be increased by increasing the ridge width. However, the growth of brightness already saturates within the domain of BRW lasers. Nevertheless, at 10 MW cm^{-2} front facet power density a lateral brightness of 2 W mm^{-1}mrad^{-1} was measured for the BRW laser with widest ridge (23 μm) which is comparable with the best values known for broad-area lasers.

To further improve the brightness of BRW lasers, higher-order modes have to be kept below threshold. This could be achieved by further reducing the lateral index guiding and therefore the number of guided lateral modes and/or other mode filter concepts which cause additional losses experienced by the higher-order modes. However, we showed that both simulation tools incorporate the physical effects needed to describe the modal turn on behaviour of CW-driven RW lasers and can therefore be used to develop and optimize those devices.

ORCID iDs

J-P Koester ⓘ https://orcid.org/0000-0001-6399-5306
A Putz ⓘ https://orcid.org/0000-0002-6497-2672
H Wenzel ⓘ https://orcid.org/0000-0003-1726-0223
H-J Wünsche ⓘ https://orcid.org/0000-0003-1710-2428
M Radziunas ⓘ https://orcid.org/0000-0003-0306-1266
H Stephan ⓘ https://orcid.org/0000-0002-6024-5355
M Wilkens ⓘ https://orcid.org/0000-0003-3966-0113
A Zeghuzi ⓘ https://orcid.org/0000-0002-5077-9281
A Knigge ⓘ https://orcid.org/0000-0002-0103-6238

References

[1] Inoue Y and Fujikawa S 2000 Diode-pumped Nd: YAG laser producing 122-W CW power at 1.319 /spl mu/m *IEEE J. Quantum Electron.* **36** 751–6

[2] Khitrov V, Minelly J D, Tumminelli R, Petit V and Pooler E S 2014 3kW single-mode direct diode-pumped fiber laser *Fiber Lasers XI: Technology, Systems and Applications* vol 8961 (SPIE) p 89610V

[3] Schulz W and Poprawe R 2000 Manufacturing with novel high-power diode lasers *IEEE J. Sel. Top. Quantum Electron.* **6** 696–705

[4] Zeghuzi A, Radziunas M, Wünsche H, Koester J-P, Wenzel H, Bandelow U and Knigge A 2019 Traveling wave analysis of non-thermal far-field blooming in high-power broad-area lasers *IEEE J. Quantum Electron.* **55** 1–7

[5] Zeghuzi A, Wünsche H, Wenzel H, Radziunas M, Fuhrmann J, Klehr A, Bandelow U and Knigge A 2019 Time-dependent simulation of thermal lensing in high-power broad-area semiconductor lasers *IEEE J. Sel. Top. Quantum Electron.* **25** 1–10

[6] Wilkens M, Fricke H W Z J, Maaßdorf A, Ressel P, Strohmaier S, Knigge A, Erbert G and Tränkle G 2018 High-efficiency broad-ridge waveguide lasers *IEEE Photon. Technol. Lett.* **30** 545–8

[7] Plisyuk S A, Batrak D V, Drakin A E and Bogatov A P 2006 Simulation of emission characteristics and optimisation of waveguiding parameters of a ridge semiconductor heterolaser to maximise the emission brightness *Quantum Electron.* **36** 1058

[8] Wenzel H, Dallmer M and Erbert G 2008 Thermal lensing in high-power ridge-waveguide lasers *Opt. Quantum Electron.* **40** 379–84

[9] Hasler K H, Wenzel H, Crump P, Knigge S, Maasdorf A, Platz R, Staske R and Erbert G 2014 Comparative theoretical and experimental studies of two designs of high-power diode lasers *Semicond. Sci. Technol.* **29** 045010

[10] Crosslight Lastip—Laser Technology Integrated Program (https://crosslight.com/products/lastip/ (Accessed: 2020-05-11))

[11] Synopsys LaserMOD—Photonic Device Design Software Tool (https://www.synopsys.com/photonic-solutions/rsoft-photonic-device-tools/active-device-lasermod.html (Accessed: 2020-05-11))

[12] PhotonDesign Harold—A hetero-structure laser diode model (https://www.photond.com/products/harold.htm (Accessed: 2020-05-11))

[13] Gajewski H, Liero M, Nürnberg R and Stephan H 2016 WIAS-TeSCA—Two-dimensional semi-conductor analysis package *Technical Report* Weierstrass Institute (https://oar.tib.eu/jspui/handle/123456789/2413)

[14] Ning C Z, Indik R A and Moloney J V 1997 Effective Bloch equations for semiconductor lasers and amplifiers *IEEE J. Quantum Electron.* **33** 1543–50

[15] Balsamo S, Sartori F and Montrosset I 1996 Dynamic beam propagation method for flared semiconductor power amplifiers *IEEE J. Sel. Top. Quantum Electron.* **2** 378–84

[16] Gehrig E and Hess O 2001 Spatio-temporal dynamics of light amplification and amplified spontaneous emission in high-power tapered semiconductor laser amplifiers *IEEE J. Quantum Electron.* **37** 1345–55

[17] Radziunas M 2016 Modeling and simulations of broad-area edge-emitting semiconductor devices *Int. J. High Perform. Comput. App.* **32** 512–22

[18] Zeghuzi A 2020 Analysis of spatio-temporal phenomena in high-brightness diode lasers using numerical simulations *PhD thesis* Humbold University of Berlin

[19] Crump P *et al* 2013 Efficient High-Power Laser Diodes *IEEE J. Selected Topics Quantum Electron.* **19** 1501211

[20] WIAS BALaser —A software tool for simulation of dynamics in broad area semiconductor lasers (https://www.wias-berlin.de/software/balaser/ (Accessed: 11-05-2020))

[21] Wenzel H and Zeghuzi A 2017 *Handbook of Optoelectronic Device Modeling Simulation* (Boca Raton, FL: CRC Press) pp 15–58

[22] Van Roosbroeck W 1950 Theory of the flow of electrons and holes in germanium and other semiconductors *Bell System Technical J.* **29** 560–607

[23] Vurgaftman I, Meyer J R and Ram-Mohan L R 2001 Band parameters for III–V compound semiconductors and their alloys *J. Appl. Phys.* **89** 5815–75

[24] Piprek J 2013 *Semiconductor Optoelectronic Devices: Introduction to Physics and Simulation* (Amsterdam: Elsevier)

[25] Wenzel H, Erbert G and Enders P M 1999 Improved theory of the refractive-index change in quantum-well lasers *IEEE J. Sel. Top. Quantum Electron.* **5** 637–42

[26] Wenzel H 2013 Basic aspects of high-power semiconductor laser simulation *IEEE J. Selected Top. Quantum Electron.* **19** 1–13

[27] Jäckel H and Guekos G 1977 High frequency intensity noise spectra of axial mode groups in the radiation from CW GaAlAs diode lasers *Opt. Quantum Electron.* **9** 233–9

[28] Agrawal G P 1988 Mode-partition noise and intensity correlation in a two-mode semiconductor laser *Phys. Rev.* A **37** 2488

[29] Yacomotti A *et al* 2004 Dynamics of multimode semiconductor lasers *Phys. Rev.* A **69** 053816

[30] Pavan S K, Lavrencik J and Ralph S E 2016 New model for mode partition noise in vcsel-mmf links based on langevin-driven spatio-temporal rate equations *J. Lightwave Technol.* **34** 3733–51

[31] Guthrie J, Tan G L, Ohkubo M, Fukushima T, Ikegami Y, Ijichi T, Irikawa M, Mand R S and Xu J M 1994 Beam instability in 980-nm power lasers: experiment and analysis *IEEE Photon. Technol. Lett.* **6** 1409–11

[32] Gordon R and Xu J 1999 Lateral mode dynamics of semiconductor lasers *IEEE J. Quantum Electron.* **35** 1904–11

[33] Achtenhagen M, Hardy A A and Harder C S 2006 Coherent kinks in high-power ridge waveguide laser diodes *J. Lightwave Technol.* **24** 2225–32

[34] Ziegler M, Tomm J W, Zeimer U and Elsaesser T 2010 Imaging catastrophic optical mirror damage in high-power diode lasers *J. Electron. Mater.* **39** 709–14

[35] Zhang Q, Xiong Y, An H, Boucke K and Treusch G 2016 Unveiling laser diode "fossil" and the dynamic analysis for heliotropic growth of catastrophic optical damage in high power laser diodes *Sci. Rep.* **6** 1–12

[36] Yamagata Y, Sato S, Yamada Y and Yamaguchi M 2018 Failure mode and lifetime analysis of 9× nm high power broad stripe laser diodes *2018 IEEE Int. Semiconductor Conf. (ISLC)* (IEEE) pp 1–2

[37] Pura J L, Souto J and Jiménez J 2020 Effect of thermal lensing and the micrometric degraded regions on the catastrophic optical damage process of high-power laser diodes *Opt. Lett.* **45** 1667–70

[38] Elattar M, Brox O, Della Casa P, Maaßdorf A, Martin D, Wenzel H, Knigge A and Crump P 2020 High-brightness broad-area diode lasers with enhanced self-aligned lateral structure *Semicond. Sci. Technol.* **35** 095011